Hindawi
Journal of Nanomaterials
Volume 2020, Article ID 7148714, 7 pages
https://doi.org/10.1155/2020/7148714

Research Article

Room Temperature Surface Modification of Ultrathin FeOOH Cocatalysts on Fe_2O_3 Photoanodes for High Photoelectrochemical Water Splitting

Yiqing Wei,[1,2,3] Aizhen Liao,[4] Lu Wang,[1,2,3] Xiaoyong Wang,[1] Dunhui Wang,[1,3] Yong Zhou,[1,2,3,5] and Zhigang Zou[1,2,3,5,6]

[1]*Department of Physics, National Laboratory of Solid State Microstructures, Collaborative Innovation Center of Advanced Microstructures, Nanjing 210093, China*
[2]*Eco-Materials and Renewable Energy Research Center (ERERC), Nanjing University, Nanjing 210093, China*
[3]*Jiangsu Provincial Key Laboratory of Nanotechnology, China*
[4]*College of Science, Xi'an University of Posts & Telecommunications, Xi'an 710121, China*
[5]*Kunshan Sunlaite New Energy Co. Ltd, Kunshan Innovation Institute of Nanjing University, Kunshan, No. 1666, South Zuchongzhi Road, Jiangsu 215347, China*
[6]*College of Engineering and Applied Science, Nanjing University, Nanjing 210093, China*

Correspondence should be addressed to Aizhen Liao; laznwnu@126.com, Dunhui Wang; wangdh@hdu.edu.cn, and Yong Zhou; zhouyong1999@nju.edu.cn

Received 25 September 2019; Accepted 11 November 2019; Published 10 January 2020

Academic Editor: Kishore Sridharan

An ultrathin FeOOH cocatalyst is deposited on α-Fe_2O_3 photoanodes in a simple room temperature immersion process for efficient photoelectrochemical (PEC) water splitting. The prepared FeOOH/Fe_2O_3 photoanode has a photocurrent density of up to 2.4 mA/cm^2 at 1.23 V versus reversible hydrogen electrode (RHE), and the photocurrent density is increased by about 160% compared to the bare Fe_2O_3 of 1.55 mA/cm^2. An obvious cathodic shift of the photocurrent onset potential from 0.661 to 0.582 V was also observed, and excellent stability was maintained with almost no deterioration for 5 h. The enhanced PEC performance is attributed to the decrease of the interfacial resistance between electrode and electrolyte and the increase of the injection efficiency of holes in Fe_2O_3.

1. Introduction

Solar-driven photoelectrochemical (PEC) water splitting has been a promising method to translate solar energy to chemical fuels, which has been widely concerned and studied [1]. In a PEC water splitting cell, the oxidation evolution reaction (OER) involves multiple electrons, resulting in a high overpotential requirement. The OER is thus the rate-determining step for PEC water splitting. Therefore, photoanode materials with broad range of light absorption, efficient charge transfer, low overpotential, and durability are necessary to construct a practical PEC device [2].

So far, lots of promising materials have been explored as photoanodes in a PEC device, such as Fe_2O_3, WO_3, $BiVO_4$, Ta_3N_5, and TiO_2 [3–8]. As a promising candidate material for PEC water splitting, α-Fe_2O_3 has advantages such as excellent stability, economical, nontoxic, appropriate band gap (~2.1 eV), high theoretical photocurrent value of 12.5 mA/cm^2, and nearly 15.8% solar-to-hydrogen efficiency (STH) [9]. However, due to the insufficient properties of α-Fe_2O_3 photoanode such as high overpotential, short hole diffusion length, and relatively low visible light absorption coefficient, the experimental solar energy conversion efficiency is still far from reaching the theoretical value [10]. Therefore, some effective strategies for improving the PEC performance of the α-Fe_2O_3 photoanode were explored, such as element doping (such as Mo^{6+}, Nb^{5+}, Ti^{4+}, Al^{3+}, Mg^{2+}, and Zn^{2+}), nanostructure regulation (such as

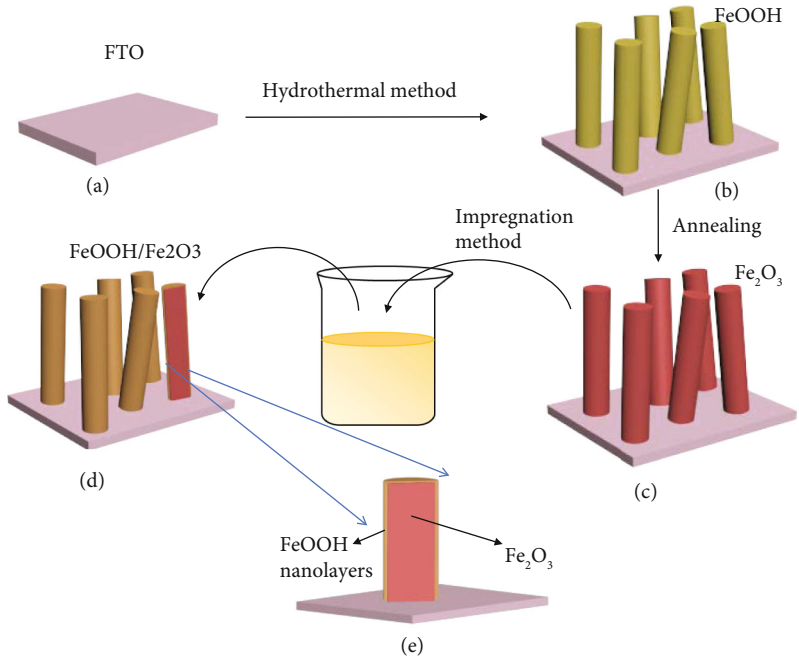

Figure 1: The schematic illustration of the synthesis procedure of $FeOOH/Fe_2O_3$.

nanobelts, nanorods, and nanowires), heterojunction building, surface passivation (such as Al_2O_3 and Ga_2O_3), incorporation of conducting scaffolds (such as ITO and graphitic carbon nitride), and deposition of oxygen evolution cocatalysts (OECs) [2, 11–14]. There is slow oxidation kinetics on the surface of α-Fe_2O_3, so the overpotential of the α-Fe_2O_3 electrode is extremely high. OEC deposition can effectively accelerate the oxidation rate of water, thereby reducing the onset potential of α-Fe_2O_3. Co-Pi and noble metal oxides (such as IrO_2 and RuO_2) are representative traditional materials applied as OECs [15]. The loading VIII metal (Fe, Co, and Ni) oxide or (oxy) hydroxide widely used as cocatalysts on photoanodes for water oxidation have proven to be an effective method [16, 17]. Among them, Fe is less toxic than Co and Ni and the most sufficient transition metal in the earth's crust [18, 19]. Meanwhile, oxyhydroxides are one of the most efficient cocatalysts in recent years for some semiconductor thin film photoanodes [20].

In this work, an FeOOH cocatalyst deposit onto Fe_2O_3 photoanodes (abbreviated as $FeOOH/Fe_2O_3$) was realized via a simple method of room temperature immersion method. Urea was added to the precursor that prepared $FeOOH/Fe_2O_3$. The urea slowly hydrolysed and formed NH_3 to enable the formation of FeOOH in the presence of Fe^{3+}. In this way, an FeOOH nanolayer can be rapidly grown on the surface of an Fe_2O_3 nanorod. The formed FeOOH cocatalyst effectively decreases the interfacial resistance between the electrode and the electrolyte of Fe_2O_3 photoanodes and increases the injection efficiency of holes. This allows the holes to travel faster from the Fe_2O_3 photoanode surface to the electrolyte, thus the efficient water oxidation reaction occurs at the interface of electrode and electrolyte. Compared with the bare Fe_2O_3 photoanodes, the photocurrent density of the $FeOOH/Fe_2O_3$ photoanodes is revealed to be considerably improved, with an increase from 1.55 to 2.23 mA/cm^2 at 1.23 V vs. RHE. Simultaneously, a cathodic shift of onset potential is about 80 mV from 0.66 to 0.58 V and excellent photostability in 5 h.

2. Experimental

2.1. Sample Preparation. The Fe_2O_3 nanorod array grows on substrate of F-doped tin oxide (FTO) transparent conductive glass, which is prepared by a simple hydrothermal method. The prepared FTO glass is ultrasonically cleaned with ultrapure water, acetone, and ethanol, respectively, for no less than 30 min. A stainless steel autoclave contains the FTO glass and 25 ml ultrapure water including 0.15 M $FeCl_3{\cdot}6H_2O$ (Shanghai Hushi, 99.99%), 90 μl $TiCl_3$ (3AChem, 15.0–20.0% $TiCl_3$ basis in 30% HCl), and 0.3 M $CO(NH_2)_2$ (Shanghai Hushi, 99%). Four pieces of cleaned FTO were placed against the wall of the autoclave. The reaction is 6 h for 100°C, then cooled to room temperature naturally. After being annealed at 550°C and 650°C in air, α-Fe_2O_3 photoanodes were prepared.

$FeOOH/Fe_2O_3$ photoanodes were formed by the room temperature impregnation method. The Fe_2O_3 photoanode was immersed in 25 ml solution of 0.075 M $FeCl_3{\cdot}6H_2O$ (Shanghai Hushi, 99.99%) and 0.15 M $CO(NH_2)_2$ (Shanghai Hushi, 99%) for varying durations (1 h, 2 h, and 3 h) at room temperature (25°C). The sample is rinsed with ultrapure water and then blown dry.

2.2. Characterization of Materials. The morphologies of the samples were observed by a scanning electron microscope (SEM) Nova Nano SEM 230 FEI Co, and a JEM-200CX TEM transmission electron microscope is used for observing transmission electron microscopy (TEM). The UV-vis spectra were observed with a UV-2550 (Shimadzu) UV-vis spectrophotometer. The crystal structures of the samples

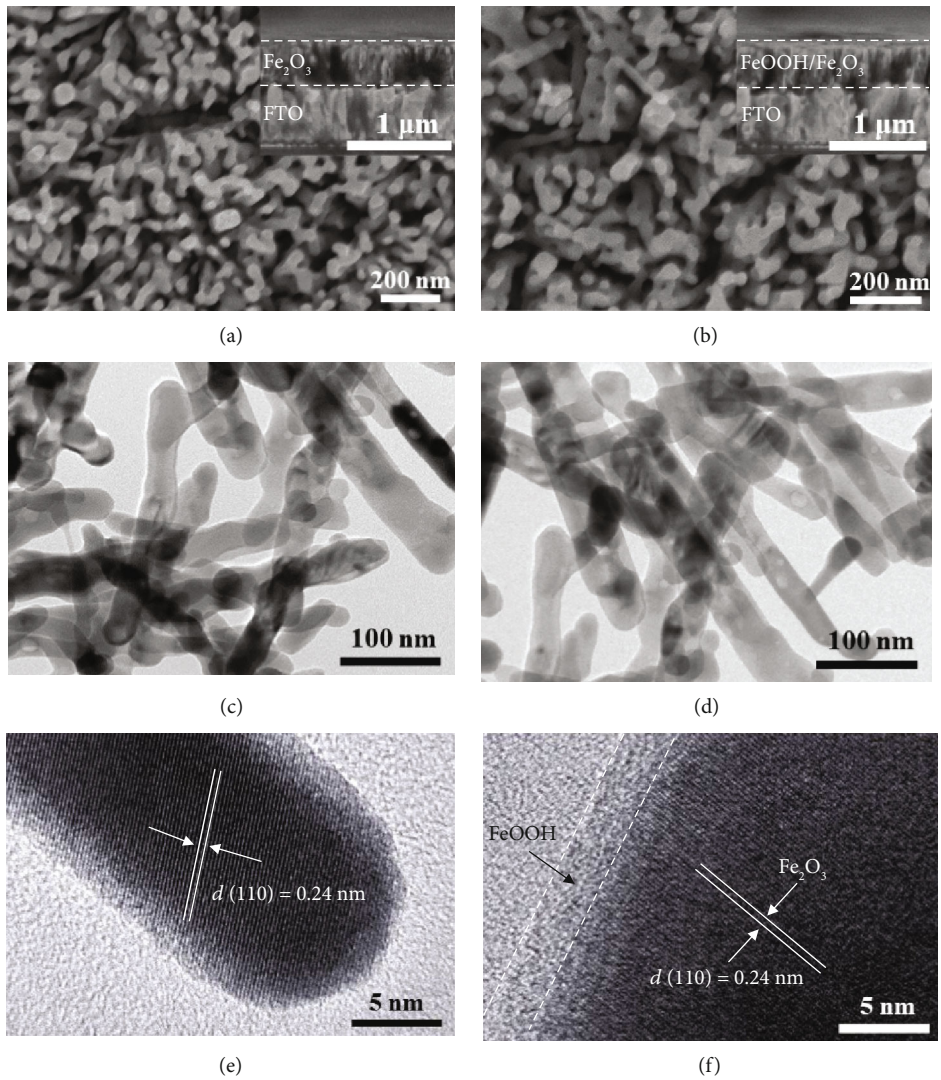

Figure 2: SEM images of (a) bare Fe_2O_3 and (b) FeOOH/Fe_2O_3 photoanodes. Low-resolution TEM images of (c) bare Fe_2O_3 and (d) FeOOH/Fe_2O_3 photoanodes. High-resolution TEM images of (e) bare Fe_2O_3 and (f) FeOOH/Fe_2O_3 photoanodes.

were examined by Ultima III Rigaku (Cu Kα radiation) X-ray diffraction (XRD). The binding energy was measured by a photoelectron spectrometer (XPS) of Thermo ESCALAB 250 X-ray and was calibrated by C1s (284.5 eV).

2.3. Photoelectrochemical Performance. The PEC test was performed under a three-electrode system using a CHI-760E electrochemical workstation manufactured by Shanghai Chenhua. The voltage scanning speed should not be too fast to prevent charging and discharging. The voltage scanning rate selected in this paper is 20 mV/s, and the range is 0.4 V to 1.8 V vs. RHE. A 500 W xenon lamp is used for the light source, and the light intensity used in this experiment is 52.7 mW/cm^2. When the photocurrent is tested, the sample is irradiated by light from the back (α-Fe_2O_3/electrolyte interface) and the exposed area of the photoanode under illumination was 0.28 cm^2. In the PEC test, the working electrode is Fe_2O_3 or FeOOH/Fe_2O_3 samples, the counter electrode is Pt electrode, and the reference electrode is Ag/AgCl electrode. A 1 M NaOH aqueous solution (pH 13.6) was used as electrolyte. The calculated formula is $V_{RHE} = V_{Ag/AgCl} + 0.059\,PH + E_{Ag/AgCl}\,V$, where V_{RHE} represents the potential versus reversible hydrogen electrode and $E^0_{Ag/AgCl} = 0.197$ V.

3. Results and Discussion

As shown in Figure 1, FeOOH nanorods were grown on FTO by the hydrothermal method to prepare the FeOOH/Fe_2O_3 photoanode. And then, a red-orange Fe_2O_3 film is obtained by high-temperature annealing (650°C) as described previously [3]. Subsequently, the α-Fe_2O_3 photoanodes are immersed in precursor aqueous solutions to allow ultrathin FeOOH to grow on the Fe_2O_3 nanorod surface. The FeOOH cocatalyst was loaded by immersing Fe_2O_3/FTO into a precursor aqueous solution of $FeCl_3{\cdot}6H_2O$ and urea at room temperature. The urea slowly hydrolysed and form NH_3 to enable the formation of FeOOH. The presence of Fe^{3+} apparently promotes the hydrolysis reaction at room temperature.

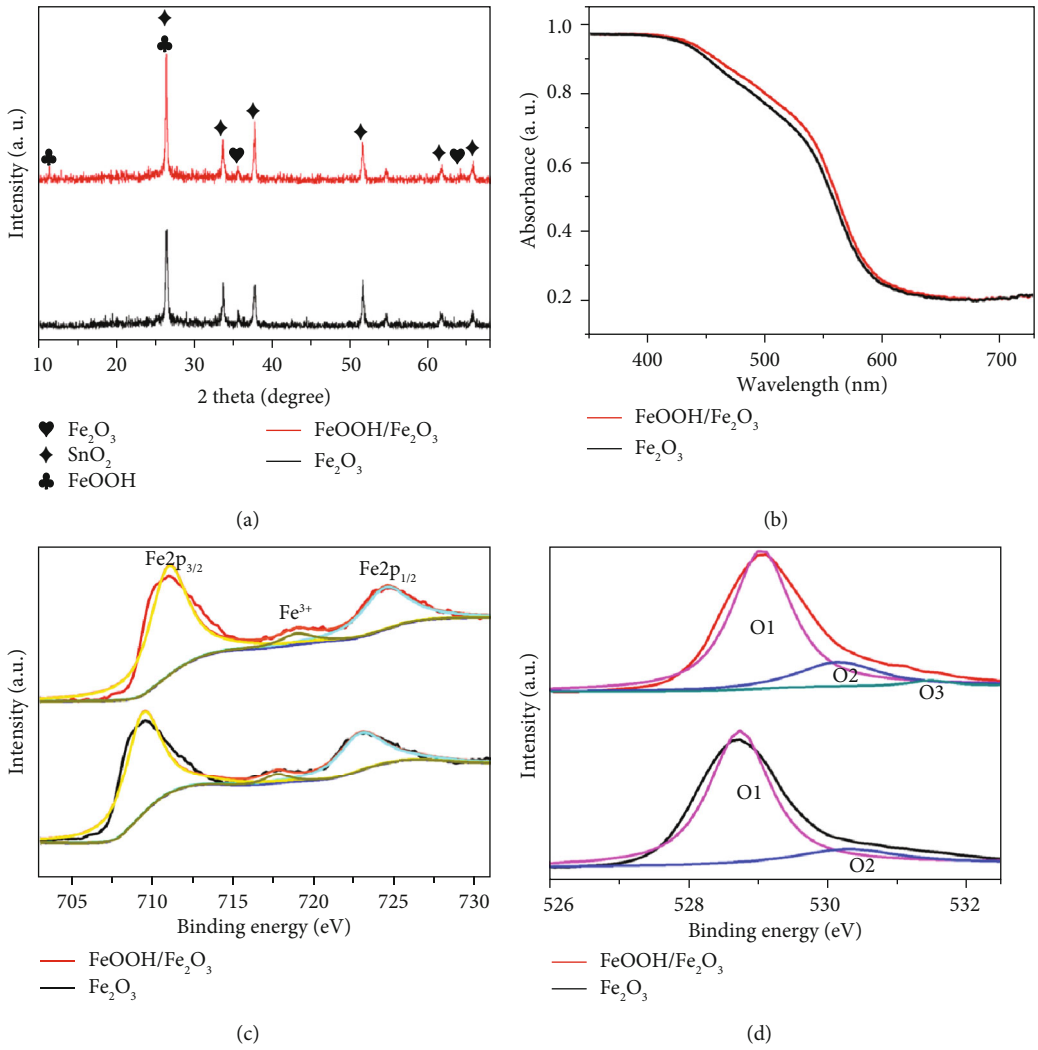

Figure 3: Corresponding XRD patterns (a) and UV-vis absorption spectra (b). High-resolution XPS spectra of (c) O1s and (d) Fe2p in Fe_2O_3 and $FeOOH/Fe_2O_3$ photoanodes.

In the SEM images (Figures 2(a) and 2(b)), both bare Fe_2O_3 and $FeOOH/Fe_2O_3$ exhibited a similar morphology. The measurement diameter is about 50 nm and the length is about 400 nm. No morphological differences between the Fe_2O_3 and $FeOOH/Fe_2O_3$ nanorod arrays were observed, which indicates that the immersion treatment of Fe_2O_3 at room temperature has no effect on the Fe_2O_3 nanorods. The low-resolution TEM images clearly show the morphologies of bare Fe_2O_3 and $FeOOH/Fe_2O_3$ nanorods (Figures 2(c) and 2(d)). As shown in Figure 2(e), high-resolution transmission electronic microscopy (HR-TEM) images show that the lattice distance was 0.24 nm, corresponding to the interplanar spacing of 110 planes of hematite (α-Fe_2O_3). Figure 2(f) shows a uniform FeOOH coating on the surface of Fe_2O_3 with a thickness of 2.23 nm. The XRD patterns of $FeOOH/Fe_2O_3$ and Fe_2O_3 exhibit diffraction peaks which are consistent with hematite (α-Fe_2O_3, JCPDS 33-0664) and F-doped tin oxide (FTO, JCPDS 41-1445) (Figure 3(a)). In addition to this, it can be found that the photoanode of $FeOOH/Fe_2O_3$ is matched with FeOOH (JCPDS No. 34-1266) by two relatively weak peaks of 11.8° and 26.7° in 2θ, respectively, detected in XRD. Figure 3(b) shows that the wavelength-dependent light absorption of $FeOOH/Fe_2O_3$ is almost the same as that of the bare Fe_2O_3 and it is only slightly higher (~3%) in the wavelength region of 450-550 nm. The nearly identical light absorption between Fe_2O_3 and $FeOOH/Fe_2O_3$ is attributed to the FeOOH ultrathin thickness. XPS spectra of the FeOOH/-Fe_2O_3 and Fe_2O_3 photoanodes show that the binding energies of Fe2p were basically the same in the two samples before and after treatment (Figure 3(c)), while the binding energies of O1s were changed (Figure 3(d)). Three binding energies (O1, O2, and O3) of O1s (529.7 eV, 530.4 eV, and 531.3 eV) are observed in Figure 4(b), belonging to the O^{2-} species, OH^- group, and adsorbed oxygen species, respectively. The XPS spectra of $FeOOH/Fe_2O_3$ show an OH^- peak with higher intensity than that of Fe_2O_3, which proved the existence of FeOOH. The above results lead to the conclusion that the ultrathin FeOOH nanolayer can be uniformly loaded on the Fe_2O_3 photoanodes successfully via a simple method of room temperature immersion method.

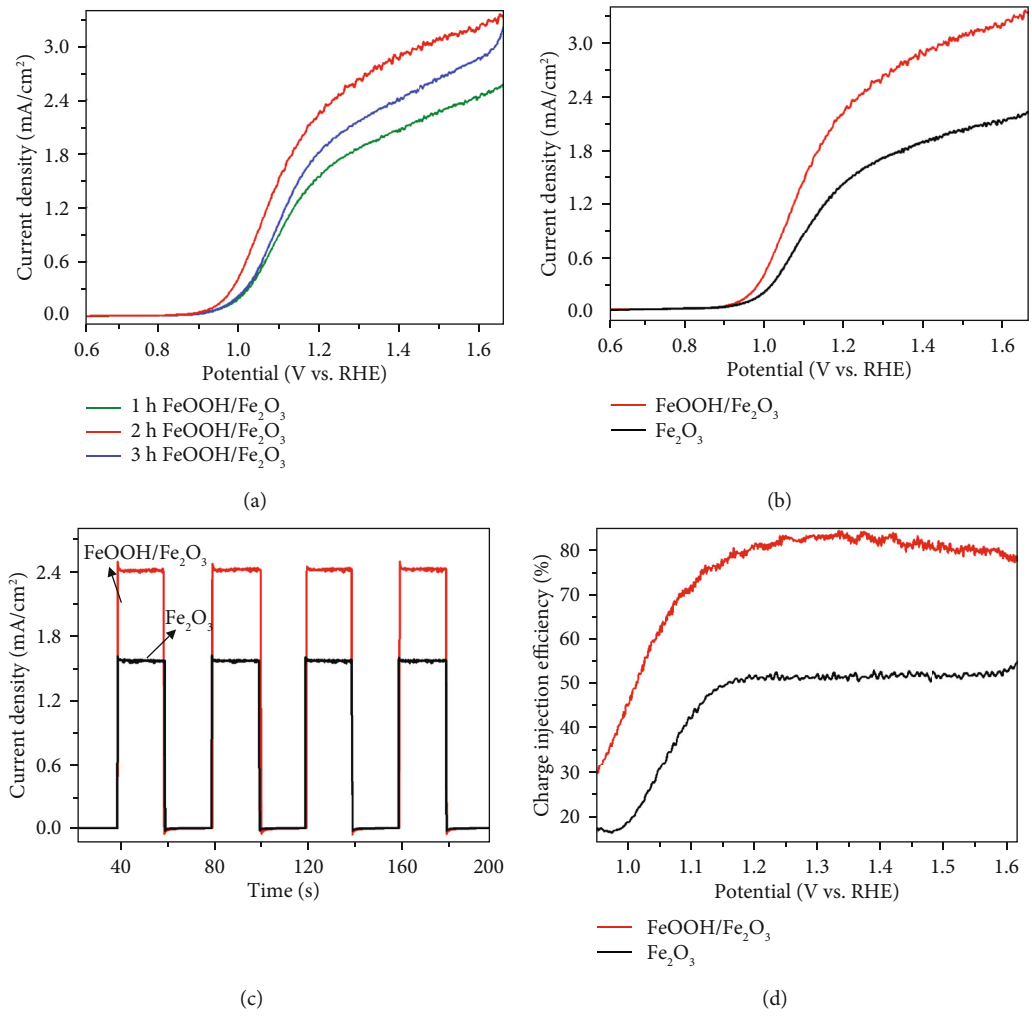

FIGURE 4: (a, b) Current density-voltage curves. (c) Transient photocurrent responses (I–t) for Fe_2O_3 and FeOOH/Fe_2O_3 samples under visible light irradiation at 1.23 V vs. RHE. (d) Injection efficiency at 1.23 V vs. RHE for the Fe_2O_3 and FeOOH/Fe_2O_3 photoanodes.

Figure 4(a) shows the photocurrent comparison of Fe_2O_3 photoanodes after different times of solution impregnation method treatment. It can be seen that the photocurrent of the two-hour treatment FeOOH/Fe_2O_3 photoanode is the highest with the lowest of starting voltage. Figure 4(b) shows the photocurrent density-potential curves of bare Fe_2O_3 and FeOOH/Fe_2O_3 photoanodes. It can be seen that compared with the bare Fe_2O_3, the FeOOH/Fe_2O_3 photoanode has a relatively enhanced photocurrent density, with an increase from 1.55 to 2.40 mA/cm^2 at 1.23 V vs. RHE. Simultaneously, the cathodic shift of onset potential with about 80 mV from 0.66 to 0.58 V is also observed. The results show that the deposition of an FeOOH ultrathin overlayer can improve the photocurrent density availably, and the onset potential of Fe_2O_3 photoanodes can be effectively decreased. The transient photocurrent response curves of photoelectrodes were acquired at 1.23 V vs. RHE under chopped light illumination (Figure 4(c)). The photocurrent intensity of FeOOH/Fe_2O_3 exhibits obviously higher than that of bare Fe_2O_3 when irradiated by the light source. The photocurrent densities obtained are basically consistent with the values from the density-potential curves at 1.23 V vs. RHE. Under on/off cyclic light illumination, the electrodes have fast light response and excellent photosensitivity. At the moment the light is turned on, the slight photocurrent transient spikes were observed, which were caused by a slight recombination of holes and electrons. The photocurrent density in a hole scavenger (0.1 M Na_2SO_3) containing electrolyte solution was conducted to clarify the charge injection efficiency of bare Fe_2O_3 and FeOOH/Fe_2O_3 photoanodes. The charge injection efficiency of FeOOH/Fe_2O_3 reached 82% at 1.23 V vs. RHE, which was obviously better than the 51% of Fe_2O_3 (Figure 4(d)). The increased charge injection efficiency contributes to the enhanced photocurrent density of FeOOH/-Fe_2O_3 photoanodes.

In order to explain the different charge transfer of the bare Fe_2O_3 and FeOOH/Fe_2O_3 photoanodes, the EIS tests are examined under the xenon lamp illumination at 1.23 vs. RHE (Figure 5(a)). Equivalent resistance and capacitance circuit model is fit to these data (Figures 5(c) and 5(d)). Here, Rs represents series resistance, which includes the resistance of interface between FTO and Fe_2O_3 films and contact

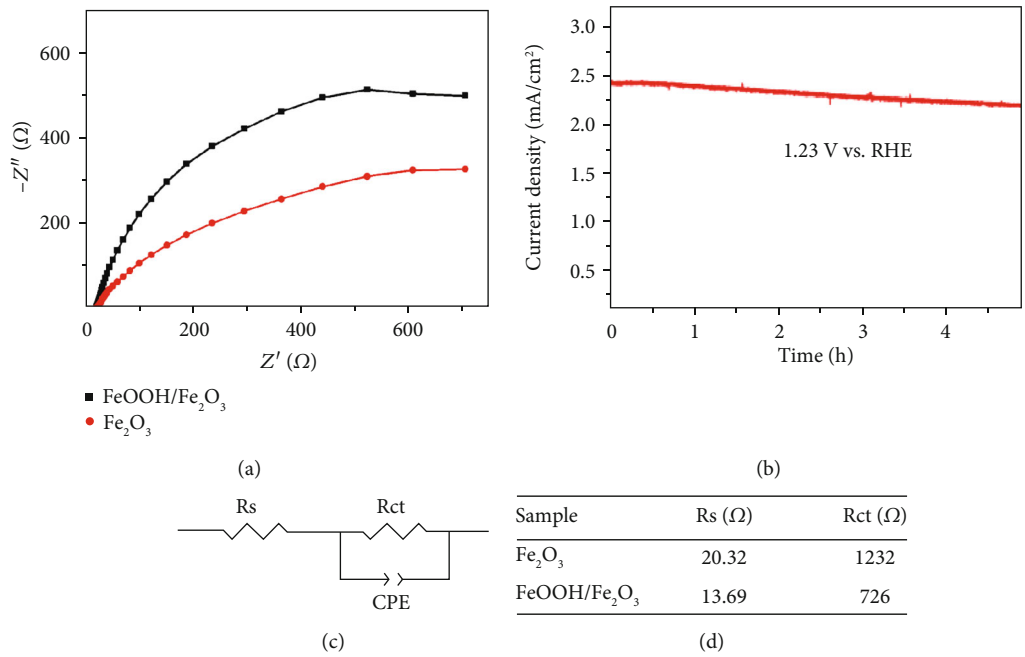

Sample	Rs (Ω)	Rct (Ω)
Fe_2O_3	20.32	1232
$FeOOH/Fe_2O_3$	13.69	726

(d)

Figure 5: (a) Nyquist plots of Fe_2O_3 and $FeOOH/Fe_2O_3$ photoanodes under xenon lamp, where the symbol and solid line represent experimental data and fitting results with (c, d) the equivalent circuit model for data fitting, as well as the fitting results. (b) Current density versus time measured at the potential of 1.23 V vs. RHE for the $FeOOH/Fe_2O_3$ photoanode.

resistance of the test system [3]. The charge transfer resistance (Rct) of the $FeOOH/Fe_2O_3$ photoanode was smaller than that of the Fe_2O_3 photoanode, which proves the faster charge transfer from the $FeOOH/Fe_2O_3$ photoanode to the electrode/electrolyte interface [21]. The reduction of resistance indicated that the FeOOH nanolayer allows that more holes are efficiently captured and promotes the hole migration on the interface of electrode and electrolyte, thus achieving an effective water oxidation reaction. As far as we know, photostability is a considerable characteristic of photoanodes, thus the photocurrent density versus time of the $FeOOH/Fe_2O_3$ photoanode was further tested. As shown in Figure 5(b), it reveals no significant attenuation under xenon lamps for 5 h in 1 M aqueous NaOH and it exhibits excellent photostability. It can also be seen that the enhancement of $FeOOH/Fe_2O_3$ photoanode photocurrent density is not caused by the photo corrosion of the photoanode and the enhanced performance of PEC is not at the expense of the stability of light.

4. Conclusions

A simple room temperature immersion method is used to form an FeOOH nanolayer on an Fe_2O_3 photoanode. The FeOOH nanolayer, as an efficient OEC, can increase the hole injection efficiency and effectively decrease the interfacial resistance between electrode and electrolyte, so the photocurrent density greatly improved, appreciably lowering the onset potential for the Fe_2O_3 photoanode. Excellent photostability is also observed. The desirable enhanced photocurrent density is 2.40 mA/cm^2 at 1.23 V vs. RHE, and the evidently lower onset potential is 0.58 V.

Data Availability

The data used to support the findings of this study are available from the corresponding authors upon request.

Conflicts of Interest

The authors declare that they have no conflicts of interest.

Acknowledgments

The study was supported by the NSF of China (No. 21773114), the NSF of Jiangsu Province (No. BK20171246), and the Fundamental Research Funds for the Central University (020414380135).

References

[1] B. Zhang, L. Wang, Y. Zhang, Y. Ding, and Y. Bi, "Ultrathin FeOOH nanolayers with abundant oxygen vacancies on $BiVO_4$ photoanodes for efficient water oxidation," *Angewandte Chemie, International Edition*, vol. 57, no. 8, pp. 2248–2252, 2018.

[2] C. Ding, J. Shi, Z. Wang, and C. Li, "Photoelectrocatalytic water splitting: significance of cocatalysts, electrolyte, and interfaces," *ACS Catalysis*, vol. 7, no. 1, pp. 675–688, 2017.

[3] A. Liao, H. He, Z. Fan et al., "Facile room-temperature surface modification of unprecedented FeB co-catalysts on Fe_2O_3 nanorod photoanodes for high photoelectrochemical performance," *Journal of Catalysis*, vol. 352, pp. 113–119, 2017.

[4] O. Zandi and T. W. Hamann, "Enhanced water splitting efficiency through selective surface state removal," *The Journal of Physical Chemistry Letters*, vol. 5, no. 9, pp. 1522–1526, 2014.

[5] S. Higashimoto, M. Sakiyama, and M. Azuma, "Photoelectrochemical properties of hybrid WO_3/TiO_2 electrode. Effect of structures of WO_3 on charge separation behavior," *Thin Solid Films*, vol. 503, no. 1-2, pp. 201–206, 2006.

[6] T. W. Kim and K. Choi, "Nanoporous $BiVO_4$ photoanodes with dual-layer oxygen evolution catalysts for solar water splitting," *Science*, vol. 343, no. 6174, pp. 990–994, 2014.

[7] Y. Li, T. Takata, D. Cha et al., "Vertically aligned Ta_3N_5 nanorod arrays for solar-driven photoelectrochemical water splitting," *Advanced Materials*, vol. 25, no. 1, pp. 125–131, 2013.

[8] V. Antonucci, E. Passalacqua, and N. Giordano, "TiO_2-based photoelectrodes in photoelectrochemical cells: performance and mechanism of O_2 evolution," *International Journal of Hydrogen Energy*, vol. 12, no. 5, pp. 305–313, 1987.

[9] A. G. Tamirat, J. Rick, A. Dubale, W. Sub, and B. Hwang, "Using hematite for photoelectrochemical water splitting: a review of current progress and challenges," *Nanoscale Horiz*, vol. 1, no. 4, pp. 243–267, 2016.

[10] B. Iandolo, B. Wickman, I. Zoric, and A. Hellman, "The rise of hematite: origin and strategies to reduce the high onset potential for the oxygen evolution reaction," *Journal of Materials Chemistry A*, vol. 3, no. 33, pp. 16896–16912, 2015.

[11] Z. Li, W. Luo, M. Zhang, J. Feng, and Z. Zou, "Photoelectrochemical cells for solar hydrogen production: current state of promising photoelectrodes, methods to improve their properties, and outlook," *Energy & Environmental Science*, vol. 6, no. 2, pp. 347–370, 2013.

[12] C. W. Scott, V. Kislon, D. Hen et al., "Identifying champion nanostructures for solar water-splitting," *Nature Materials*, vol. 12, no. 9, pp. 842–849, 2013.

[13] S. D. Tilley, M. Comuz, K. Sivula, and M. Gratzel, "Light-induced water splitting with hematite: improved nanostructure and iridium oxide catalysis," *Angewandte Chemie, International Edition*, vol. 49, no. 36, pp. 6405–6408, 2016.

[14] A. Naseri, M. Samadi, A. Pourjavadi, A. Z. Moshfegh, and S. Ramakrishna, "Graphitic carbon nitride ($g\text{-}C_3N_4$)-based photocatalysts for solar hydrogen generation: recent advances and future development directions," *Journal of Materials Chemistry A*, vol. 5, no. 45, pp. 23406–23433, 2017.

[15] Y. Park, K. J. McDonald, and K. S. Choi, "Progress in bismuth vanadate photoanodes for use in solar water oxidation," *Chemical Society Reviews*, vol. 42, no. 6, pp. 2321–2337, 2013.

[16] H. Li, Y. Gao, Y. Zhou et al., "Construction and nanoscale detection of interfacial charge transfer of elegant Z-scheme $WO_3/Au/In_2S_3$ nanowire arrays," *Nano Letters*, vol. 16, no. 9, pp. 5547–5552, 2016.

[17] S. Li, Y. Wang, S. Peng et al., "Co-Ni-based nanotubes/nanosheets as efficient water splitting electrocatalysts," *Advanced Energy Materials*, vol. 6, no. 3, article 31501661, 2016.

[18] R. L. Lee, P. D. Tran, S. S. Pramana et al., "Assembling graphitic-carbon-nitride with cobalt-oxide-phosphate to construct an efficient hybrid photocatalyst for water splitting application," *Catalysis Science & Technology*, vol. 3, no. 7, pp. 1694–1698, 2013.

[19] F. Zhang, A. Yamakata, K. Maeda et al., "Cobalt-modified porous single-crystalline $LaTiO_2N$ for highly efficient water oxidation under visible light," *Journal of the American Chemical Society*, vol. 134, no. 20, pp. 8348–8351, 2012.

[20] J. Kim, D. Youn, K. Kang, and J. Lee, "Highly conformal deposition of an ultrathin FeOOH layer on a hematite nanostructure for efficient solar water splitting," *Angewandte Chemie International Edition*, vol. 55, no. 36, pp. 10854–10858, 2016.

[21] G. Ge, M. Liu, C. Liu et al., "Ultrathin FeOOH nanosheets as an efficient cocatalyst for photocatalytic water oxidation," *Journal of Materials Chemistry A*, vol. 7, no. 15, pp. 9222–9229, 2019.